ELSEVIER

Contents lists available at ScienceDirect

Powder Technology

journal homepage: www.journals.elsevier.com/powder-technology



Combined imaging and chromatic confocal microscopy technique to characterize size and shape of ensembles of cuboidal particles

Petros Neoptolemou^a, Thomas Vetter^{a,1}, Aurora J. Cruz-Cabeza^b, Ashwin Kumar Rajagopalan^{a,*}

- ^a Department of Chemical Engineering, The University of Manchester, Manchester M13 9PL, United Kingdom
- ^b Department of Chemistry, University of Durham, South Road, Durham, DH1 3LE, United Kingdom

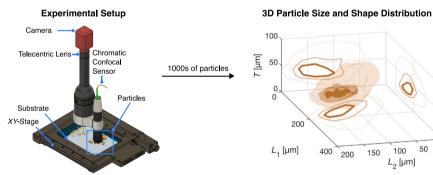
HIGHLIGHTS

Imaging and confocal microscopy for size and shape characterization of powders.

- Technique provides three characteristic lengths for 1000s of cuboidal particles.
- Accurate and rapid 3D characterization of particle size and shape distribution.
- Complements existing process analytical technology to evaluate solid form products.

GRAPHICAL ABSTRACT





ARTICLE INFO

Keywords:
Powder
Crystallization
Imaging
Confocal microscopy
Particle size distribution
Particle shape

ABSTRACT

The presence of needle- and plate-like particles has detrimental consequences on their downstream processing in the fine chemicals sector. Therefore, the ability to accurately characterize the particle size and shape is essential to quantify and predict their impact on the product processability. Nonetheless, tools to characterize both the size and shape of ensembles of cuboidal particles are seldom available. The overarching goal of this work is to provide a fast and accurate offline size and shape characterization tool. To this aim, we have designed and experimentally validated a combined imaging and chromatic confocal microscopy technique. We propose two modes of operation: one that facilitates the accurate 3D reconstruction of particles; and the other that facilitates their rapid characterization. We validate the performance of our technique using a commercial technique. We show that our technique can accurately characterize thousands of particles, making it a valuable addition to existing process analytical technology.

1. Introduction

Particle size and shape distribution (PSSD) impacts processing, handling and end-product quality of powders [1] in several sectors including sedimentology [2], food industry [3], agriculture [4], fine chemicals [5], materials science [6] and magnetism [7]. In the fine

chemicals sector, the PSSD has an impact on the packing density [8], thermal conductivity [9], filtration performance [10–12], flowability [13,14], dosing [15,16], tabletability [17], dissolution rate [18] and solubility [19], to name a few. As a result, there has been a significant momentum over the last two decades to alter the PSSD using techniques

E-mail address: a.rajagopalan@manchester.ac.uk (A.K. Rajagopalan).

https://doi.org/10.1016/j.powtec.2023.119032

Received 30 July 2023; Received in revised form 23 September 2023; Accepted 27 September 2023 Available online 3 October 2023

0032-5910/© 2023 The Author(s). Published by Elsevier B.V. This is an open access article under the CC BY-NC-ND license (http://creativecommons.org/licenses/by-nc-nd/4.0/).

^{*} Corresponding author.

¹ Current Address: Department of Solid Form Science, H. Lundbeck A/S, Ottiliavej 9, 2500 Copenhagen, Denmark

that employ controlled cooling crystallization [20,21], milling [22–24], temperature cycling [25–28], additives [29–33], or a combination of these. To facilitate the evaluation of the effect of the aforementioned techniques on the PSSD, being in possession of an accurate and robust tool to characterize the particle size and shape is a key prerequisite.

Traditionally, it is common practice in both an academic and an industrial setting to measure a single characteristic length of the particles [34], often assuming a spherical shape for any arbitrarily shaped particle. Tools such as the resistive pulse sensing, focused beam reflectance measurement and laser diffraction have been applied to monitor processes aimed at altering the particle size distributions [24,35-37]. To allow monitoring of the particle shape, some efforts have been invested in obtaining multiple characteristic lengths from chord length distributions, but with moderate success [38-42]. Other size characterization techniques for powder and biomass materials such as sieving or elutration can be employed to undertake a physical particle size separation. However, these methods require considerable amounts of material for the analysis, which can pose challenges when employed in fine chemical industries, where sample quantity is limited during the research and development phase [43]. Spherical approximation of particles, often used in these approaches, has been shown to give an insufficient characterization especially in cases where the particles exhibit a needle- or plate-like shape [44].

To obtain multiple characteristic lengths, the most widely available and ideal approach involves employing imaging techniques. Over the years, single- and dual-projection imaging techniques, both online and offline, have been employed to obtain two characteristic lengths for elongated particles [28,45–51], a shape which is often observed in crystallization processes. The adoption of imaging techniques to characterize the PSSD has led to undertaking process modeling for the description of fundamental phenomena like growth, dissolution, milling, and process design and control for the manipulation of both the particle size and shape [12,21,27,32,52–59]. Interested readers are directed to three recent reviews on crystalline particle [60,61] and soil particle [62] characterization techniques and their applications.

Cuboidal, especially plate-like, particles are also often encountered alongside elongated particles. To accurately characterize such particles, using a simple geometric model, one requires three characteristic lengths, i.e., length, width, and thickness. X-ray Computed Tomography (XCT) [62-68], offline stereoscopic imaging [69,70], digital holography [71] and fluorescence confocal microscopy combined with image processing [72] are some of the techniques that are capable of accurate 3D reconstruction of single or several particles. Despite their ability to fully reconstruct the 3D shape, these techniques have associated disadvantages in terms of the minimum resolution or the time taken to characterize an ensemble of particles. Techniques such as white light interferometry [73], laser scanning confocal microscopy (LSCM) [62, 74], and more recently the DISCO [75,76] are able to estimate the three characteristic lengths of ensembles of particles. However, white light interferometry finds it challenging to measure particles with low reflectivity. The LSCM gives superior resolution and can completely reconstruct the 3D shape, but is relatively slow and could take in the order of hours to characterize a population of a few thousand particles. These two issues associated with the reflectivity and measurement time are tackled by the DISCO, which was built to characterize the size and shape of crystal populations in real-time in an order of few minutes. Alas, given the design and the operation of the DISCO, which is a dualprojection imaging setup, the accuracy of the measurement is closely tied to the particle orientation with respect to its two cameras [75]. Therefore, the end-user has to choose between speed and accuracy of the measurement.

To address the aforementioned shortcomings, we have conceptualized and built an offline characterization device which combines two independent techniques: single-projection imaging and chromatic confocal microscopy. The former is used to detect and estimate two of the three characteristic lengths, i.e. the length and the width of

crystals dispersed on a substrate [47]. The latter, chromatic confocal sensor (CCS), is used to estimate the third characteristic length, i.e. the thickness of the crystals [77]. The resolution along the thickness of the particles for the CCS is as high as LSCM, but in contrast the CCS measurement can be modified to become faster than the LSCM measurement. Additionally, as the particles are dispersed on a substrate, the effect of particle orientation on the accuracy of the measurement, as observed with the DISCO, is circumvented. Therefore, the proposed technique can complement traditional offline techniques used both in an academic and industrial setting, to provide a more accurate and faster characterization of cuboidal particles.

The article is structured as follows. First, in Section 2, we provide an overview of the proposed technique, hardware, and software used to obtain the particle size and shape of cuboidal particles. Second, in Section 3, we explain the methods used to obtain ensembles of cuboidal particles used in the experimental studies. Third, in Section 4, we evaluate the performance of the proposed technique in terms of its accuracy by comparing the measurements with a commercial technique. Finally, in Section 5, we present a rapid characterization of the size and shape of cuboidal particles using our proposed technique and evaluate its performance both in terms of time and accuracy.

2. Measurement device

In this section, we provide the conceptual working of the combined camera and chromatic confocal sensor (CCS) setup (Section 2.1), the hardware (Section 2.2) and the software framework (Section 2.3) of the proposed technique. The terms particle, crystal and object are used interchangeably, as well as, height and thickness.

2.1. Overview of the proposed technique

The proposed technique combines a camera for the identification and 2D characterization of crystals dispersed on a substrate, as explained elsewhere [47], with a chromatic confocal sensor (CCS) to obtain the third characteristic length leading to a 3D characterization. The CCS provides a single-point measurement which can be utilized to characterize surface roughness, surface thickness, and reconstruct 3D profiles of round and freeform surfaces [78]. Within the context of characterizing PSSDs of crystalline powders, CCS has never been used.

A typical CCS setup is composed of a light source, a beam splitter, a lens, and a filtering pinhole. Light from a chromatic light source incident on a lens, is dispersed to its visible colors, resulting in a cone of light. This cone of light is characterized by the different wavelengths at different distances, as visualized in Fig. 1. A spectrometer detects the reflected light from the sample and when an object is in the measuring range of the CCS, its surface is visible as a high intensity peak. Since the distance from the object is proportional to the wavelength of the reflected light, it is possible to calibrate the position of a given point within the measuring range with nanometer accuracy (usually calibrated by the CCS manufacturer).

Since the aforementioned workflow provides the thickness or height of the particle only at a single point, to scan an area, one can implement a translational mechanical motion [79]. Here, the sensor scans multiple points on the object to obtain a topographic image. In this work, the translational motion is achieved through a motorized XY-stage. Subsequently, using the signal obtained by the CCS from the object and the substrate (Fig. 1), we can calculate the object's thickness.

In contrast to the usual applications of CCS-based microscopy, in our application we need to scan thousands of particles, dispersed over an area of a few thousand square millimeters. This is an overwhelmingly large area to scan with a micro-scale XY resolution. We circumvent this issue through a two-step process. First, we detect the particles in our substrate using the imaging camera and we map their location on the XY plane. Second, we use the CCS to scan only the area that includes the identified particles. This avoids scanning the area on the substrate that is free of any particles and leads to saving in excess of 90% of the scanning time.

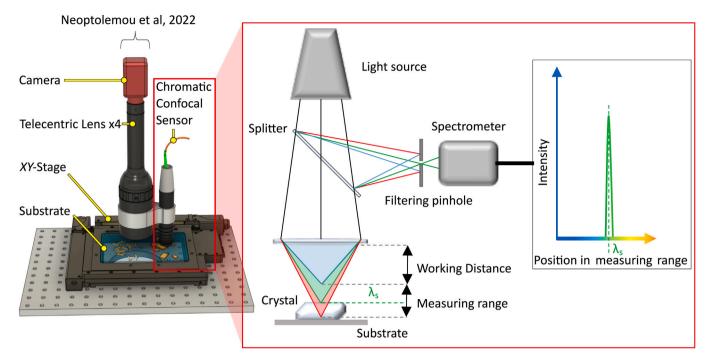


Fig. 1. Schematic of the proposed combined imaging and chromatic confocal microscopy setup. The key contribution from this work stems from the addition of a chromatic confocal sensor to a previously reported imaging setup [47]. In this sensor, a light source is sent through a splitter and subsequently directed to a chromatic dispersive lens. The resulting cone of light from the lens, incident on a particle/surface, leads to different wavelengths focused at different heights. The light reflected from the surface is analyzed using the spectrometer and using a predefined calibration, the height of the surface is obtained. The combined imaging and chromatic confocal microscopy setup facilitates a 3D reconstruction of particles.

2.2. Hardware

A schematic of the proposed technique is shown in Fig. 1. An additional photograph of the setup illustrating the full list of parts is shown in Figure S1 in the Supplementary Material. Prior to the measurement, the crystalline powder (≈25 mg) is dispersed with air at 2 barg on an acrylic substrate (The University of Manchester workshop, Manchester, England) using a custom built powder disperser [47]. The substrate is then placed on a XY-stage (ASR100B120B-E03, Zaber Technologies Inc., Vancouver, Canada). A linear Z-stage (X-LSM050-E, Zaber Technologies Inc., Vancouver, Canada) is used to focus on the dispersed particles in the image captured by the camera (Basler ace acA2440-20gm Monochrome GigE Camera, Basler AG, Ahrensburg, Germany). A magnifying lens (4.0X SilverTL magnifying lens, Edmund Optics, York, England), is attached to the camera, which is backlit illuminated using a telecentric backlight illuminator (60 mm, Edmund Optics, York, England), through an opening in the breadboard (Thorlabs LTD, Ely, England) that holds the setup. The resulting real-world size (i.e., combined camera-lens system) of the pixels is $0.8625\,\mu m$ \times $0.8625\,\mu m$. The Z-stage holds the CCS (model DT2405-3, Micro Epsilon UK LTD, Birkenhead, England) attached alongside the camera. The CCS has a spot size of 9 µm, a measuring range of 3 mm, a working distance of 20 mm, a Z-resolution of 40 nm, and is operated with an exposure time of 2500 µs to accurately characterize low reflecting crystal surfaces. The XY-stage is programmed to move in a squarewave pattern to obtain images using the camera/lens system. Subsequently, upon detection of the crystals, using the protocol discussed in Section 2.3, the Z-stage moves to bring the particle within the measuring range of the CCS. This step of moving the Z-stage is repeated for all the particles within the scan area.

To evaluate the accuracy of the aforementioned technique, the size and shape characterization measurements of particle populations were compared to the ones obtained from laser scanning confocal microscopy, LSCM (VK-X200, Keyence, Osaka, Japan). The objective lens with the smallest magnification, 10x, was used for LSCM, which

has a field of view of $1350\,\mu m \times 1012\,\mu m$. Each topographic image was obtained at the lowest resolution of 1024×768 pixels for high speed scans with a vertical step size of $4\,\mu m$. The laser source has a wavelength of 408 nm (violet).

2.3. Software

In this section, the data acquisition and data processing of the CCS and the LSCM measurements are described. Due to the differences in the software of the instruments, the data acquisition steps of both the techniques differ significantly. However, to facilitate a fair comparison of the results obtained from the two techniques, the data processing approach employed is similar.

Data acquisition. The data acquisition (step A to E) and data processing (step F and G) methodology used in this work is visualized in Fig. 2. First, for the proposed setup, grayscale images of a predefined area are acquired using the camera (step A). Second, the grayscale images are binarized (step B) using the imbinarize function from the Image Processing Toolbox of MATLAB [80], which performs a background separation by employing Otsu's method to calculate a global threshold [81]. Third, the binarized images are stitched to form a single image of the predefined area (step C) using the methodology explained elsewhere [47]. Fourth, the boundaries of the connected objects on the images are identified using the bwboundaries function from the Image Processing Toolbox of MATLAB [80] and a rectangular box is fitted around each of them, shown in red (step D). To ensure that the imaged particle is inside the scanned area and to acquire sufficient points from the surface of the substrate for baselining, the CCS scans an area larger than the area of the rectangular box shown in step D. Since the CCS acquires data from a single spot, the XY-stage performs a squarewave motion, composed of 30 lines as shown in step E(a), simultaneously recording the [X,Y] position and the time t. As the stage moves, the CCS records the distance r of the surface from the sensor as a function of time t, as shown in step E(b). In contrast to the LSCM measurement, due to the design of the proposed setup, the

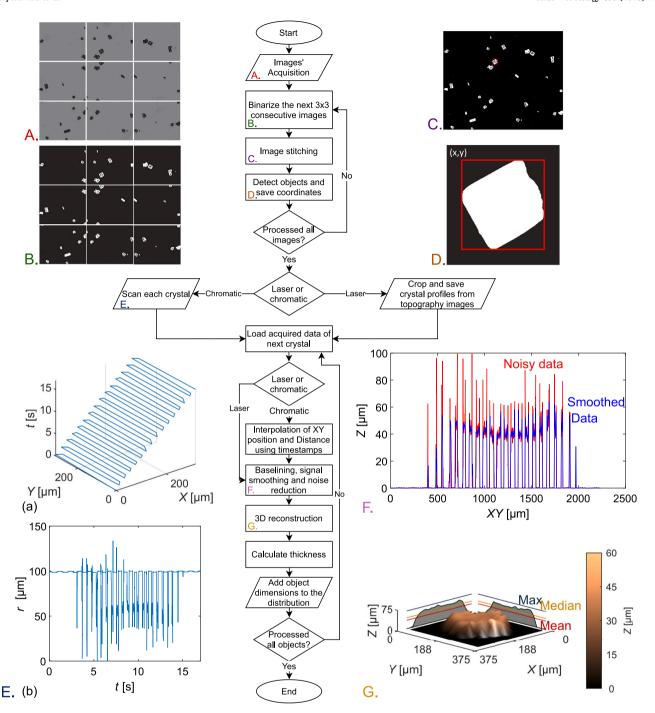


Fig. 2. Flowchart illustrating the data acquisition and data processing steps for the proposed technique (CCS) and the laser scanning confocal microscopy (LSCM). Examples of each of the key steps (A through G) from real experiments are also provided alongside. Data acquisition involves **(A)** acquiring grayscale images from the camera (CCS) or height map (LSCM), **(B)** binarizing images (CCS and LSCM), **(C)** stitching the binarized images (CCS and LSCM), **(D)** locating the crystals in the binarized image (CCS and LSCM), and **(E)** finally, scanning each particle by the chromatic confocal sensor using a squarewave motion of the *XY*-stage and obtaining the height map, i.e. height *r* vs. time *t* (CCS). Data processing involves **(F)** preprocessing the height data by performing a noise removal and **(G)** eventually, reconstructing the 3D shape of the imaged particle and evaluating different thickness metrics (CCS and LSCM).

XY position and the distance r are obtained from two independent devices at different frequencies. Thus, the data from the two sensors is interpolated with respect to time t, using the interp2 function of MATLAB, to 3D reconstruct the scanned particle.

In LSCM, the acquisition of data is slightly different, i.e. a topographic image (height map) of a large scanned area (including the empty space in-between particles) is obtained. The topographic image (step A) is then converted to a binary image (step B). The binary images are subsequently stitched (step C) and then the particles are separated from the background. A rectangular box is fitted around each imaged

particle (step D). Finally, the location of the detected crystals is used to obtain the height map of individual particles from the scanned area.

Data processing. After the height data is obtained from both techniques, several data processing steps are undertaken. First, a baseline correction is applied. As seen in Fig. 2E (b), the raw data obtained from the sensor corresponds to the distance to the object that first reflects the light (this distance equals the position in the measuring range mentioned in Fig. 1). This could either be the surface of the particles or the surface of the substrate. Hence, to obtain the thickness

of the actual particle, the distance to the particle is subtracted from the distance to the substrate (in this example the substrate is at \approx 100 μm). To identify the points that correspond to the substrate and to the particle, Otsu's method using the multithresh function from the Image Processing Toolbox of MATLAB is employed [80]. This classifies the acquired points into two groups: a group with larger distances that corresponds to the substrate; and one with smaller distances that corresponds to the particle. Subsequently, a plane is fitted through the points corresponding to the substrate using the pcfitplane function from the Computer Vision Toolbox of MATLAB [82]. Using the fitted plane as a reference, all the acquired data points are baseline corrected. This baseline correction also helps correct any errors arising from a tilted substrate. An identical processing is also performed for the height maps acquired from LSCM. Second, a noise removal step is applied on all the acquired data (step F). This is required as the data from CCS and LSCM measurements can be noisy due to the reflection from the edges of the particles and/or long exposure times of the sensor. To this aim, a combination of moving median and moving average filters is applied on the reshaped XY vs. Z data using the movmedian and movmean functions of MATLAB, respectively.

Particle reconstruction and characterization. Finally, using the preprocessed data from the sensors, the particle is reconstructed in the 3D space and three characteristic lengths are computed (step G). First, the length L_1 and width L_2 are simply obtained by fitting an areaconserved bounding box on the projections of particles from the camera, using the methodology described elsewhere [47]. Second, the thickness is obtained from the height data of the CCS/LSCM measurements. Any object thinner than $2\,\mu m$ (cut-off) is discarded from the measurement. In this work, we have assigned a specific thickness to a particle by using the maximum M, the median m or the mean μ of the preprocessed height data for each particle.

The final output, i.e. the 3D reconstruction along with the projections, of three crystals of three different compounds (see Section 3 for production methodology) using the proposed technique and LSCM is shown in Fig. 3. Note that these crystals have different sizes and shapes. Based on the reconstruction and the extracted thickness (using three different metrics) from the two techniques, it must be evident the resulting outcome is qualitatively comparable. Despite the data preprocessing step, some of the peaks observed in the reconstruction cannot be avoided and in most cases these can be attributed to noise in the measurement.

3. Materials

Commercially available steel feeler gauges (Hotop, Hong Kong) were used to provide a first comparison of the measurement accuracy (see Section 4.1). Single crystals of tolfenamic acid (Fluorochem LTD, Hadfield, England, 98.0%) and benzoic acid (Sigma-Aldrich, Gillingham, England, 99.0%) were used to compare the 3D reconstructed particles from the two techniques (see Section 4.1). Crystals of tolfenamic acid form IX were crystallized from solution using the methodology described previously [83] and crystals of benzoic acid were obtained by crystallizing them from water by slow evaporation. Finally, the comparison of 3D reconstruction, of individual size and shape characteristics and of distributions between the proposed technique and LSCM were evaluated using three different crystalline compounds (see Sections 4.1 and 4.2). We used (a) L-ascorbic acid (Sigma-Aldrich, Gillingham, England, 99.0%) as received from the manufacturer and sieved (75 μm to 150 μm); (b) benzamide (Sigma-Aldrich, Gillingham, England, 99.0%) recrystallized from isopropanol (Honeywell UK LTD, Bracknell, England, 99.5%) by crash cooling from 40 to 20 °C; and (c) aspirin (Sigma-Aldrich, Gillingham, England, 98.0%) grown in ethanol (VWR Chemicals, Lutterworth, England, 99.9%) by slow linear cooling (40 to 20 °C in 4 h).

4. Performance evaluation of the proposed imaging technique

Here, we evaluate the accuracy of our proposed technique by comparing it with the measurements obtained using the well established laser scanning confocal microscopy (LSCM), using the methodology described in Sections 2.2 and 2.3, by undertaking an experimental campaign. First, in Section 4.1, we perform a one-to-one comparison of the size and shape characteristics obtained from the two techniques on steel feeler gauges and single crystals. We subsequently rationalize the choice of the thickness metric to be used to characterize the third length of the particles. Second, in Section 4.2, we present the 3D PSSDs and 1D thickness distribution of three populations (of three model compounds) that exhibit different size and shape characteristics.

4.1. Evaluation of individual size and shape characteristics

In this section, we perform a one-to-one comparison of the size and shape characteristics obtained from the CCS and LSCM on different systems. First, we compare the two techniques by measuring the thickness of steel feeler gauges whose actual thickness ranges from $40\,\mu m$ to $80\,\mu m$. Second, we compare the 3D reconstruction of millimetersized single crystals of benzoic acid (angled with rough surface) and tolfenamic acid (smooth and low reflective surface). Third, we compare the size and shape characteristics of hundreds of individual crystals of L-ascorbic acid, benzamide, and aspirin.

For the first test, we used three feeler gauges with a thickness of $40\,\mu m$, $50\,\mu m$, and $80\,\mu m$. Since we could not obtain a certification for their accuracy, we used the LSCM measurements as reference. Following the data acquisition and processing methodology described in Sections 2.2 and 2.3, with our proposed technique we obtained thicknesses of 43.2, 50.0, and 76.6 μm , while with the LSCM we obtained thicknesses of 42.5, 54.1 and 73.6 μm . The 3D reconstruction of these three cases for the two techniques are illustrated in Figure S2 in the Supplementary Material. These results show that the measurement outcome from the two techniques are comparable and we observe a maximum deviation of 4 µm between them. We have found that this can be affected by two factors. First, in contrast to LSCM, the CCS measurement is performed while the XY-stage is moving. Therefore, any vibration from the stage can introduce measurement errors. Second, the highly reflective surface of the gauges leads to more noise on the CCS data than the LSCM. The former problem is unavoidable, however, it leads to a negligible error. While the latter does not exist when dealing with crystalline particles due to their low reflective surface.

For the second test, we compare the size and shape characteristics, through the 3D reconstruction of millimeter-sized benzoic acid and tolfenamic acid crystals obtained from the two techniques. The reconstructed crystals are visualized in Fig. 4. To facilitate a fair comparison, we rebinned the height maps along the X and the Y dimensions for both the techniques (panels c through f) with a bin size of 50 µm. Subsequently, the mean height of the points that constitute a given bin is visualized. Apart from the actual height in each bin, we also computed the difference in the mean height (in each bin) ΔZ obtained from the two techniques (panels g and h) to identify regions of the particle that might have poor measurement accuracy. It must be evident that if both techniques have identical performance, then $\Delta Z = 0$. From Fig. 4, we can make two observations. First, qualitatively the shape of the crystals imaged from the two techniques appear identical. Second, the difference in the height obtained from the two techniques is close to 0 µm for the bulk of both crystals (silver region). However, we can observe differences between the two techniques close to the edges of the crystals. This difference can be attributed to two factors. First, for the characterization of the two crystals presented here, a lower XY resolution coupled with the inherent noise associated with the techniques leads to bigger variation in computing the average height in a given bin. Second, unlike CCS, the LSCM has the ability to measure steeper angles (with limitations for low reflective surfaces [84]). This

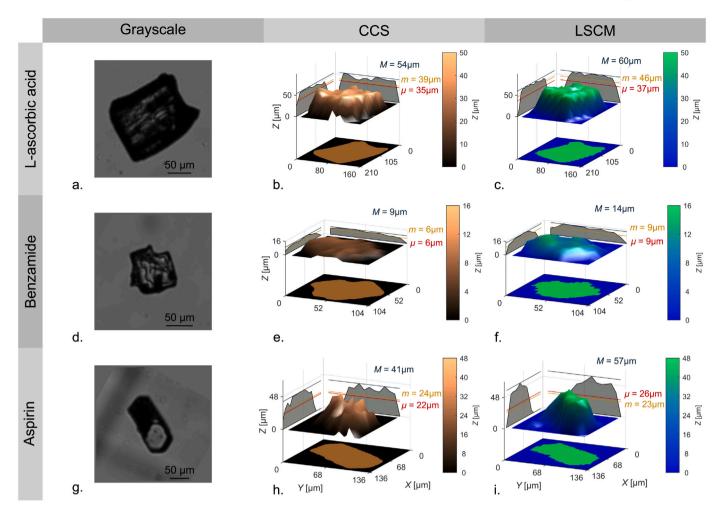


Fig. 3. Grayscale images (Grayscale, left panels), 3D reconstruction and thickness obtained from the proposed technique (CCS, middle panels) and laser scanning confocal microscopy (LSCM, right panels), using the approach discussed in Sections 2.2 and 2.3, for (**a**, **b**, **c**) ι-ascorbic acid, (**d**, **e**, **f**) benzamide, and (**g**, **h**, **i**) aspirin. The corresponding thickness metrics, maximum *M*, median *m*, and mean *μ*, extracted from the height map of particles are highlighted alongside the projections.

might lead to an inaccurate surface profiling of single particles when using CCS, especially at the edges as seen in the case of tolfenamic acid. As would be made clear through the discussion presented in the subsequent sections, the discrepancies observed here are acceptable as the bulk of the crystal is characterized to a very good accuracy using the proposed technique.

For the third test, we compared the area, convexity, circularity, and thickness, of hundreds of individual crystals of the three chosen model compounds. Note that the same crystal was imaged using both techniques. The former three characteristics are visualized through parity plots in Fig. 5, obtained using equations provided in Section S3 in the Supplementary Material. We can make four observations. First, in terms of the size of the particles (inferred from the projected area in panel a), L-ascorbic acid crystals have the biggest size followed by aspirin and benzamide. This is also confirmed by the scanning electron microscopy (SEM) images provided in Fig. 6. Second, we see that the projection area obtained from our setup $A_{\mathbb{C}}$ is slightly bigger than the one from the LSCM $A_{\rm L}$. This can be attributed to differences in the optics and data acquisition employed in the two techniques. The camera combined with the telecentric lens and illumination in the proposed technique provides a sharper distinction between the object and the background when compared to the low contrast, low resolution, and front-lit topography image from the LSCM measurement. Third, due to the underestimation of the area from the LSCM, the length L_1 and width L_2 will also be underestimated. This is reflected by the square root of the area from the two measurements (see panel a)

that serves as a proxy to the two quantities. Fourth, the agreement on the other two shape descriptors convexity CX and circularity CR (see Section S3 in the Supplementary Material for definitions) between the two techniques is poorer when compared to the area. The reason for this discrepancy can again be attributed to the quality of the images obtained from the LSCM. This effect will be particularly exacerbated when dealing with faceted crystals instead of rectangular prisms.

The comparison of the thickness, obtained from the two techniques, for the particles used in the aforementioned analysis is visualized as parity plots in Fig. 6. As mentioned in Section 2.3, we obtained the maximum M, the median m, and the mean μ using the preprocessed height data. We can make three observations. First, the L-ascorbic acid crystals are thicker when compared to the other two compounds. Second, irrespective of the metric and the compound, the thickness evaluated for all the crystals lie around the y = x line. This indicates a good agreement between the thickness evaluated from the proposed technique and the LSCM measurements. Third, the deviation ϵ , which quantifies the average distance of the points to the y = x line for each thickness metric, reveals that the thickness evaluated using the mean μ has the least deviation and using the maximum M has the highest deviation. The higher deviation associated with the maximum is expected for two reasons: (a) the inability to completely remove the spikes in the signal during the noise removal step (Fig. 2 step F) and (b) the ability of detecting certain peaks arising due to surface roughness, by either of the two techniques (see Fig. 3f, where the mean μ and median m are identical but the maximum M is off).

P. Neoptolemou et al.

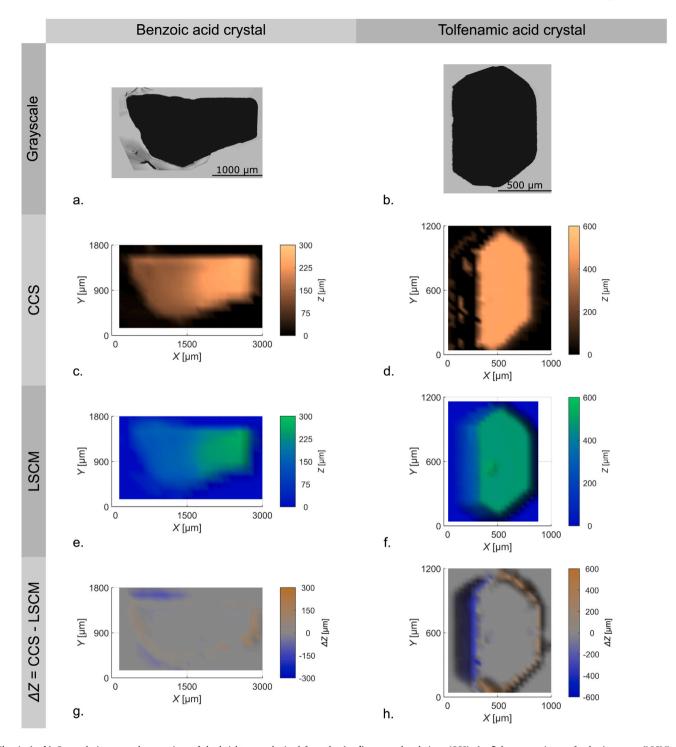


Fig. 4. (a, b) Grayscale images and comparison of the height map obtained from the (c, d) proposed technique (CCS), (e, f) laser scanning confocal microscopy (LSCM), and (g, h) difference in the height ΔZ obtained between the two techniques for millimeter-sized benzoic acid crystal (left panels) and tolfenamic acid crystal (right panels) using the approach discussed in Sections 2.2 and 2.3. In panels c through h, along both the X and the Y dimensions, a constant bin width of $50 \, \mu m$ was used.

Based on the analysis presented in this section, we can conclude that the accuracy of the proposed technique, both in terms of the area and the thickness, is in good agreement with the commercial LSCM measurements. Also, the analysis – as expected – revealed that using the mean of the height data obtained from individual crystals exhibits lower differences between the two techniques when compared to the median or the maximum. Therefore, in the next section, we will be using the mean as the thickness metric to compare the 3D PSSD and 1D thickness distributions.

4.2. Evaluation of 1D and 3D distributions

In this section, we present the comparison of the distributions obtained by characterizing ensembles of particles of different systems from the two techniques. First, we compare the 3D PSSDs (i.e. accounting for length, width, and thickness) of three compounds obtained from the proposed technique with the PSSDs obtained from the LSCM measurements, using the methodology described in Sections 2.2 and 2.3. Second, given the focus of the work on accurately characterizing the thickness of the particles, we also compare the 1D thickness

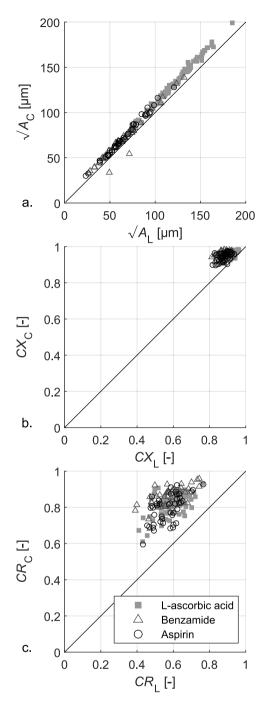


Fig. 5. Parity plot of **(a)** square-root of projected area $\sqrt{A_i}$, **(b)** convexity CX_i , and **(c)** circularity CR_i , obtained using equations provided in Section S3 in the Supplementary Material, for the proposed technique (CCS, i = C) and laser scanning confocal microscopy (LSCM, i = L) for several single crystals of 1-ascorbic acid (square markers), benzamide (triangular markers), and aspirin (circular markers).

distributions of the aforementioned ensembles obtained from the two techniques. The typical distribution consists of $\approx 40\,000$ particles for the CCS measurements and ≈ 7500 particles for the LSCM measurements. Here, we compare both the number- and volume-weighted 3D PSSDs and 1D thickness distributions of the three model compounds, i.e. L-ascorbic acid, benzamide, and aspirin. The choice of the type of distribution and the corresponding properties depends on the application, e.g. kinetic parameter estimation, process control, to name a few [85,86]. Note that the number-weighted distributions are more sensitive to changes in the number of fines, when compared

Table 1 Number- and volume-weighted mean length \overline{L}_1 , width \overline{L}_2 , and thickness \overline{T} of the 3D-PSSDs from the proposed technique (CCS) and the laser scanning confocal microscopy (LSCM)

		\overline{L}_1 [μ m]		\overline{L}_2 [μ m]		\overline{T} [μ m]	
		LSCM	CCS	LSCM	CCS	LSCM	CCS
L-ascorbic acid	N-weighted	120.9	121.4	83.4	83.6	34.3	34.5
	V-weighted	162.0	179.9	113.7	124.2	48.2	52.2
Benzamide	N-weighted	62.0	68.6	44.8	49.2	12.9	11.3
	V-weighted	91.1	103.8	68.2	77.4	21.3	19.7
Aspirin	N-weighted	122.1	116.6	59.1	59.4	26.0	24.3
	V-weighted	210.0	207.5	103.1	103.5	46.9	42.5

to the volume-weighted distributions. Therefore, factors such as noise in the measured data and resolution of the measurement device can significantly affect the number-weighted distribution.

3D particle size and shape distributions. The discretized normalized 3D PSSDs and the corresponding 2D marginal distributions for ensembles of L-ascorbic acid, benzamide, and aspirin crystals are visualized in Fig. 7. The corresponding mean aspect ratios $\overline{L}_1/\overline{L}_2$, $\overline{L}_1/\overline{T}$, and $\overline{L}_2/\overline{T}$ is provided alongside the marginal distributions from the proposed technique (brown) and the LSCM measurement (blue). The definitions to compute these distributions are provided in Section S4 in the Supplementary Material. We can make four observations. First, for all the compounds, both the number- and volume-weighted distributions obtained from the two techniques are qualitatively identical. Second, the aspect ratios from all the distributions obtained using the two techniques are comparable. Third, based on the aspect ratio values it must be evident that all the three compounds exhibit a plate-like shape (i.e. $L_1 > L_2 \gg T$). The 1-ascorbic acid population consists mostly of large and chunky particles, hence both number- and volumeweighted distributions are shifted toward larger sizes. The benzamide population consists mostly of small particles shifting both numberand volume-weighted distributions toward smaller sizes. Finally, the aspirin population, due to a broad distribution of sizes with significant amount of small particles, leads to a number-weighted distribution that is shifted toward smaller sizes and volume-weighted distribution that is shifted toward bigger sizes. These observations are also confirmed by the SEM images presented in Fig. 6.

The number- and volume-weighted means \overline{L}_1 , \overline{L}_2 and \overline{T} of the 3D distributions for the three compounds from the two measurement techniques are provided in Table 1. Based on the values, it must be clear that the means obtained from the two techniques are comparable. The largest deviation in number-weighted mean length \overline{L}_1 is $\approx 7 \, \mu \mathrm{m}$ (benzamide), width \overline{L}_2 is $\approx 5 \, \mu \mathrm{m}$ (benzamide), and thickness \overline{T} is $\approx 2 \, \mu \mathrm{m}$ (aspirin). The corresponding deviation in volume-weighted quantities are $\approx 17 \, \mu \mathrm{m}$ (L-ascorbic acid), $\approx 11 \, \mu \mathrm{m}$ (L-ascorbic acid), and $\approx 5 \, \mu \mathrm{m}$ (aspirin), respectively. Note that on a relative scale, these values translate to less than 10% deviation between the two techniques. The reason for these discrepancies can again be attributed to the factors described in the previous section. For the sake of brevity, the corresponding analysis on the broadness of the distributions is provided in Table S1 in the Supplementary Material and they exhibit a deviation which is as low as the deviation presented here for the mean values.

1D thickness distributions. The discretized normalized 1D thickness distributions for the ensembles of L-ascorbic acid, benzamide, and aspirin crystals, reported above are visualized in Fig. 8. The corresponding distribution properties D10 (triangular marker), \overline{T} (5-pointed star marker), and D90 (6-pointed star marker) are highlighted in the plot and are provided in Table S2 in the Supplementary Material. We can make four observations. First, the distributions obtained from both the techniques are qualitatively identical. Second, the average distribution properties obtained from both the techniques are comparable. Third, both L-ascorbic acid and aspirin exhibit a broad distribution of thickness.

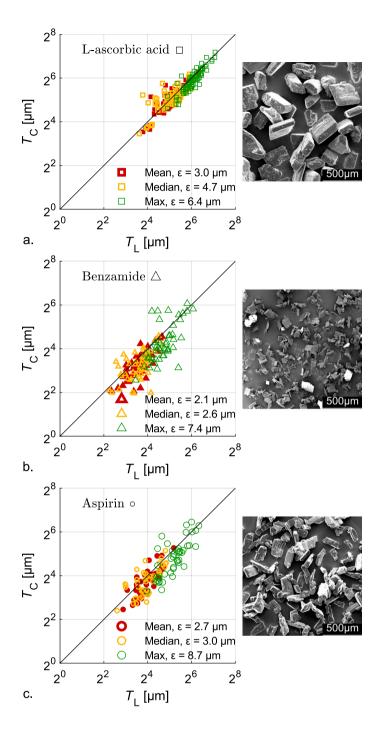


Fig. 6. Parity plot of thickness T_i of several single crystals of (a) L-ascorbic acid, (b) benzamide, and (c) aspirin obtained for the proposed technique (CCS, i = C) and laser scanning confocal microscopy (LSCM, i = L). Three different thickness metrics, namely, maximum M (green markers), median m (yellow markers), and mean μ (red markers) are visualized for each model compound along with the deviation ϵ , evaluated as the average distance of the points to the y = x line. A representative SEM image for each model compound is also provided.

While benzamide has a narrow distribution with smaller thickness when compared to the other two compounds. Finally, when calculating the V-weighted thickness distributions, the differences in the area of the particles measured with the two techniques will be transferred into these distributions as well. According to Fig. 5, our technique always gave larger areas when compared to the LSCM. This in turn will bias the V-weighted thickness distribution to higher values. This is evident from the overestimation of the V-weighted D90 of the L-ascorbic acid and aspirin. In contrast, this effect is less pronounced for D10 due to the smaller volume of particles.

Based on the comparison of the distributions presented in this section, we can conclude that the proposed technique can accurately characterize the 3D PSSD of cuboidal particles. Despite the differences in the sizes and shapes, and optical properties of the compounds, we have conclusively shown that our device can be applied to different systems thereby proving its general applicability. However, it must be kept in mind that accurate characterization of size and shape is just one half of the puzzle. The other half is the speed of data acquisition and processing. This forms the basis of the discussion presented in the next section.

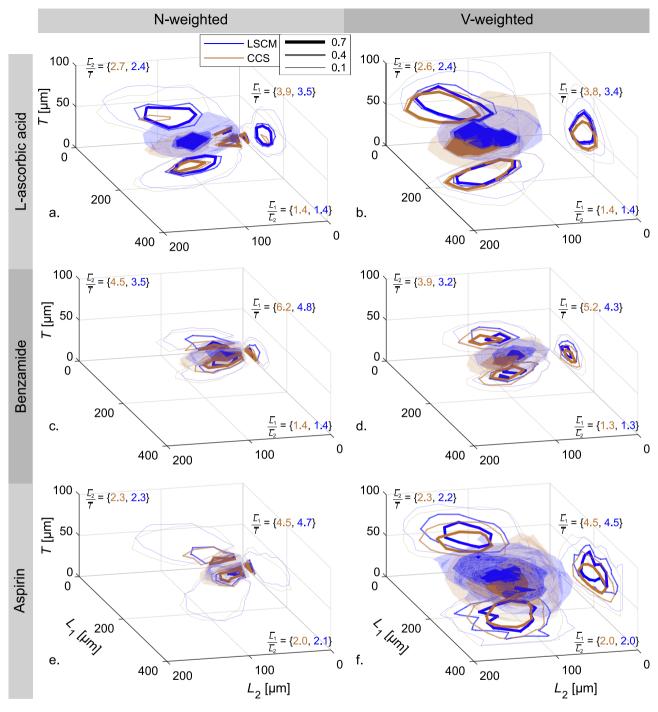


Fig. 7. Discretized normalized number- (left panels) and volume-weighted (right panels) 3D-PSSDs, evaluated using equations provided in Section S4 in the Supplementary Material, from the proposed technique (CCS, brown) and laser scanning confocal microscopy (LSCM, blue), for (\mathbf{a}, \mathbf{b}) L-ascorbic acid, (\mathbf{c}, \mathbf{d}) benzamide, and (\mathbf{e}, \mathbf{f}) aspirin. The corresponding 2D marginal distributions, obtained using equations provided in Section S4 in the Supplementary Material, and aspect ratio $\left[\overline{L}_1/\overline{L}_2\ \overline{L}_1/\overline{T}\ \overline{L}_2/\overline{T}\right]$ is highlighted alongside the 3D PSSDs. The contour lines correspond to 0.1, 0.4 and 0.7 of each distribution. In all the panels, a constant bin size of $24\,\mu\text{m}$, $24\,\mu\text{m}$, and $12\,\mu\text{m}$ was used along the L_1 , L_2 , and T dimensions, respectively

5. Toward a faster size and shape characterization of cuboidal particles

In this section, we present a faster approach using our technique to characterize the size and shape of cuboidal particles. To this aim, we propose a *single-line scan* using the CCS, instead of the *full scan* consisting of 30 line scans, used till this point following the methodology described in Sections 2.2 and 2.3, to obtain the thickness of the particles. In the previous section, we have shown that our technique can detect and accurately characterize the size and shape of cuboidal

particles by performing a *full scan*. These measurements can be time consuming when characterizing thousands of particles, as will be clear from the discussion presented below. Therefore, to speed this up, we can use a *single-line scan*, instead of 30 line scans, passing through the centroid of each particle, to obtain the third characteristic length, i.e. thickness. The other two characteristic lengths, L_1 and L_2 , can be obtained from the camera, as was the case with the *full scan*. Here, we will analyze both the speed improvement (Section 5.1) and the accuracy (Section 5.2) offered by the *single-line* scan when compared to the *full scan* and the LSCM measurements.

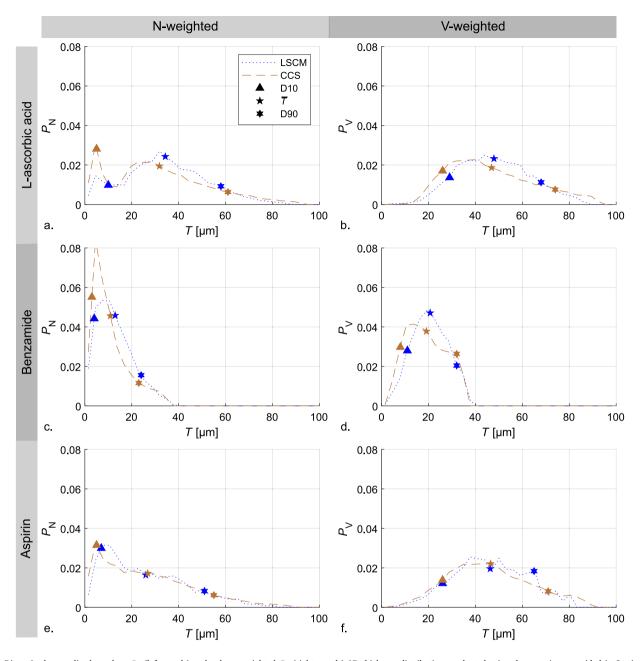


Fig. 8. Discretized normalized number- P_N (left panels) and volume-weighted P_V (right panels) 1D thickness distribution, evaluated using the equations provided in Section S4 in the Supplementary Material, from the proposed technique (CCS, brown) and laser scanning confocal microscopy (LSCM, blue), for (\mathbf{a}, \mathbf{b}) \mathbf{i} -ascorbic acid, (\mathbf{c}, \mathbf{d}) benzamide, and (\mathbf{e}, \mathbf{f}) aspirin. The corresponding distribution properties, namely, 10th percentile (D10, triangular marker), 90th percentile (D90, 6-pointed star marker), and the mean (5-pointed star marker) of the thickness distribution \overline{T} are provided alongside. In all the panels, a constant bin width of $3\,\mu\mathrm{m}$ was used.

5.1. Characterization time benefits of a single-line scan

To evaluate the time improvement in characterizing the particles using the *single-line scan*, we performed a computational study. We evaluated the overall data acquisition time $t_{\rm m}$ for 50 000 crystals dispersed on a substrate with area $A_{\rm m}$ for each of the three techniques (LSCM, CCS *full scan*, CCS *single-line scan*). To obtain the time in a computational setting, we first randomly assigned a location to each of the 50 000 particles. In our computational study, we do not assume the particles to have a specific size or shape, instead they are assumed to be a point. In reality, these points can serve as a proxy for the centroid of the particles. Subsequently, we quantify the times that correspond to each technique. For our proposed technique, we approximated $t_{\rm m}$ as the sum of the image acquisition time, traveling time, and scan time. The image acquisition time was assumed to be 1 min cm⁻². The speed of the *XY*-stage while moving from one particle to the next (in this case one point

to the next) was assumed to be $2\,\mathrm{mm\,s^{-1}}$. Therefore, with availability of the total distance to be traveled to characterize all the particles, we can find the total traveling time. We calculate the total distance by implementing an algorithm that provides a rough approximation to the shortest path to scan all the particles. Since, the thickness is not evaluated yet, the image acquisition and the traveling time will be the same for both *single-line scan* and *full scan*. Finally, the scan time of each *single-line scan* was assumed to be at a constant $0.25\,\mathrm{s}$. Thereby, the scan time of the *full scan*, with 30 lines will be 7.5 s. Note that the values reported above and the approach employed is comparable to the one used in all the experimental measurements reported in Section 4. For the LSCM measurement, the data acquisition speed was assumed to be $24\,\mathrm{min\,cm^{-2}}$. This was obtained from experimental measurements and it corresponds to the setting that leads to the fastest traveling speed from one frame to the next, lowest lateral resolution,

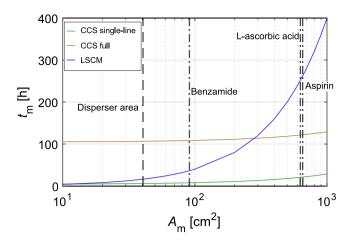


Fig. 9. Overall data acquisition time $t_{\rm m}$ to computationally characterize 50 000 particles, using the methodology described in Section 5.1, for our proposed technique (CCS) using the *full scan* (brown) and *single-line scan* (green), and the laser scanning confocal microscopy (LSCM, blue). The area of the disperser used in the experimental setup (dashed lines) and the measurement area corresponding to the experimental populations of 1-ascorbic acid, benzamide, and aspirin (dashed–dotted lines), characterized in Section 4, are displayed alongside.

and the least number of confocal scans. Here, it is fair to point out that LSCM could potentially be made faster in comparison to its current commercial implementation. This can be achieved by adjusting the scanning algorithm to measure only areas of interest, i.e., areas where particles have been located in a preliminary scan in line with what we have proposed in this work for our technique. Since it is a commercial product, we were not in a position to explore this avenue in the context of the present research.

In the results discussed below, the data acquisition time $t_{\rm m}$ was evaluated over a range of measurement area $A_{\rm m}$. The different measurement areas correspond to scenarios that lead to different particle densities i.e., number of particles per area of substrate. This area will change from one population to the other, due to different size and shape characteristics. The powder disperser used in our setup has an upper limit on the sample volume that can be dispersed to ensure a uniform dispersion [47].

The overall data acquisition time of the measurement $t_{\rm m}$ of 50000 particles for all the three techniques computed over a range of measurement area $A_{\rm m}$, based on the approach described above, is shown in Fig. 9. Two observations can be made. First, as expected, increasing the measurement area $A_{\rm m}$ increases the overall data acquisition time $t_{\rm m}$ for all the three techniques. The increase in the acquisition time for the LSCM measurement is more pronounced when compared to the two CCS scanning methods. This is attributed to the need to scan the whole area, instead of scanning solely the particles as in the case of our proposed technique. While for the case of our proposed technique, as the measurement area increases, the contribution of scanning time stays constant and only the travel time increases as the particles are dispersed further apart. Second, as expected, undertaking a *single-line scan* offers a significant reduction in the data acquisition time – almost an order of magnitude – when compared to the *full scan*.

In addition to the above analysis, we have also identified the measurement area corresponding to the experimental populations that were characterized in Section 4. The areas corresponding to these cases, highlighted using dashed-dotted lines, are also additionally shown in Fig. 9. It should be evident based on the discussion presented in the previous section that due to the smaller size of benzamide particles, the area required to disperse 50 000 particles is smaller than L-ascorbic acid and aspirin. We can make two important observations. First, the LSCM measurement is faster than the *full scan* using our proposed technique when measuring the benzamide population. In contrast, the

opposite is observed when measuring the L-ascorbic acid and aspirin populations. The behavior for the latter two cases can be attributed to the larger empty area between the particles in the images, which leads to a larger area for the LSCM device to scan. This is circumvented for the proposed technique, as the empty area between the particles is not characterized by the CCS. Second, in all three cases the *single-line scan* is the fastest option. The data acquisition time for LSCM and the *single-line scan* are comparable, when the measurement area $A_{\rm m}$ tends to very small values. However, note that this case would be unrealistic, as it becomes physically challenging to disperse 50 000 particles – sized in the micrometer range – in an area smaller than the disperser area (dashed line) without a high degree of particle overlapping.

The overall data acquisition time for the *single-line scan* was not simulated at the fastest conditions. Hence, there is more room for improvement: (a) by decreasing the time for a *single-line scan*; (b) by increasing the traveling speed; and (c) by applying a time-optimal algorithm to compute the shortest traveling route. Nevertheless, it must be clear that the *single-line scan* using our proposed technique provides significant time benefits for the size and shape characterization. Keeping this in mind, in the next section we will evaluate the measurement accuracy of the *single-line scan* and compare it with the other two techniques.

5.2. Measurement accuracy of a single-line scan

In the previous section, we have shown that the *single-line scan* can provide significant time benefits. In this section, we will evaluate the measurement accuracy of the *single-line scan* and explore the effect of measurement errors arising from four factors, namely, (a) number of data points obtained per particle from the CCS; (b) orientation of the particle projection; (c) error in the particle position resulting from the systematic error in the position of the *XY*-stage; and (d) shape of the particles. Here, we will address this by simulating the *single-line scan* at different angles and different points on the surface of the particles for the three experimental model compounds, and compare it to the *full scan* (from Section 4).

To simulate the height data obtained from the single-line scan, first, we extracted the CCS points from the full scan (see Section 4.2) of the three experimental model compound populations. Subsequently, we simulate the single-line scan, by taking the CCS points on a single line at various angles θ and various displacements D from the centroid of the particle, as highlighted using the green lines shown in Fig. 10 (panels a and b). First, we simulated the single-line scan at constant $D = 0 \,\mu\text{m}$ with varying values of θ of $[0^{\circ} 45^{\circ} 90^{\circ} 135^{\circ}]$, where $\theta = 0^{\circ}$ corresponds to the single-line scan being parallel to the X-axis of the XY-stage. Second, we simulated the *single-line scan* at constant $\theta = 0^{\circ}$ with varying values of D of $[0 \mu m 4 \mu m 8 \mu m 16 \mu m]$. Here, the lateral error should not be more than 16 µm (according to the manufacturer), therefore, this condition of D serves as a worst case scenario. Note that the data processing of the single-line scan is identical to the full scan, i.e., noise removal is performed on the raw height data, as shown in step F of Fig. 2. Since there is a single line of points across each particle from the single-line scan, a 3D reconstruction is not possible. Therefore, the thickness is calculated using the mean of the preprocessed height data, as it was decided to be the most reliable thickness metric in Section 4.1.

Discretized normalized number-weighted 1D thickness distributions from the *full scan* (dashed brown) and simulated *single-line scan* (green), of the three experimental model compounds at constant D and constant θ , are illustrated in Fig. 10. As the errors are more clearly highlighted, we compare the number-weighted instead of the volume-weighted distributions. We can make four observations. First, for both cases, the thickness distribution obtained from *single-line scan* is in good qualitative agreement with the *full scan*. Second, the thickness distributions obtained from the *single-line scan* simulated at various angles θ are nearly identical with the *full scan*. This was expected as the crystals have equant-shaped projections i.e., squares in the cases

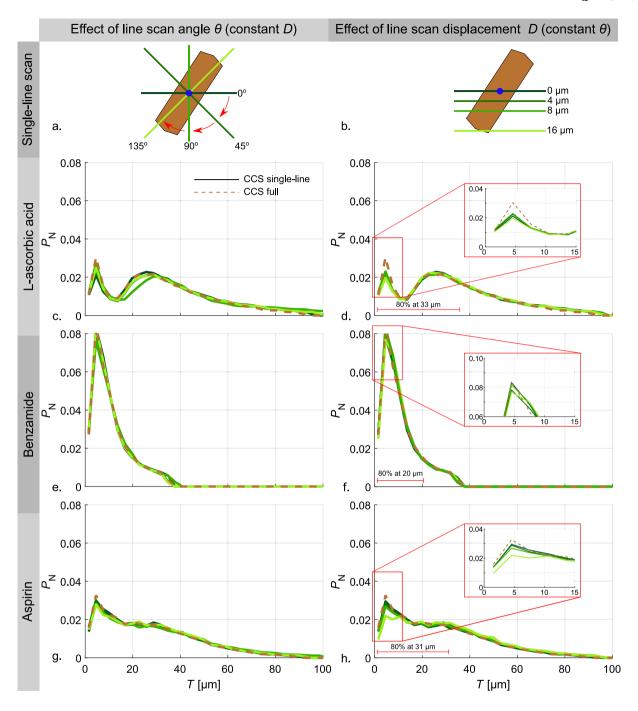


Fig. 10. Discretized normalized number-weighted 1D thickness distribution P_N , obtained using the equations provided in Section S4 in the Supplementary Material, from the full scan (brown) and the single-line scan (green) of our proposed technique (CCS), for (c, d) ι-ascorbic acid, (e, f) benzamide, and (g, h) aspirin. The panels on the left visualize the distributions obtained at a constant line scan displacement D i.e., varying line scan angle θ (0° to 135°, shades of green) along with a representative schematic of conditions obtained at a constant line scan angle θ i.e., varying line scan displacement D (0μm to 16μm, shades of green) along with a representative schematic of conditions simulated (panel b). In panels d, f, and h, the red range line indicates the size range where 80% of the particles are discarded in the case of single-line scan. In all the panels, a constant bin width of 3μm was used.

of L-ascorbic acid and benzamide, and low-aspect ratio needles in the case of the aspirin. Third – even though not evident from the figure – for all the populations, the <code>single-line</code> scan leads to fewer particles (8%–10% less) being characterized when compared to the <code>full</code> scan. This can be attributed to fewer CCS scan points, arising from a single-line, being used to compute the mean height. Hence, a large number of small particles (<20 μ m) will be discarded and if not, there will be significant uncertainty in estimating the height accurately. This effect is pronounced when the thickness distributions are broad, as in the case of L-ascorbic acid and aspirin. In these two cases, 80% of the

discarded particles (red range line shown in panels d and h) are below 33 μm and 31 μm , respectively, which is roughly 30% of the overall span ($\approx 100\,\mu m$) of the distribution. In the case of benzamide, 80% of the discarded particles (red range line shown in panels f) are below 20 μm , which is roughly 70% of the overall span ($\approx 35\,\mu m$) of the distribution. Therefore, the normalized thickness distribution of benzamide appears less affected – despite the loss in the particles – when compared to the other two compounds. Finally, due to the same reasons presented here, the effect of D is more visible when compared to the effect of θ . This is true especially for the cases of L-ascorbic acid and aspirin,

when compared to benzamide. We can see that the probability density of the former two compounds at smaller sizes ($< 20 \,\mu\text{m}$) decreases with an increase in displacement *D* (see zoomed-in area in panels d and h).

In the study presented in this section, the movement of the XY-stage was simulated such that it moves parallel to the X-axis during each single-line scan, thereby providing height data at $\theta = 0^{\circ}$, as shown in panel a of Fig. 10. Note that particles with a high aspect ratio along L_1 and L_2 with a thin L_2 (e.g. acicular particles), could potentially lead to measurements with a higher error when compared to the ones presented here. This can be attributed to the low amount of height data that would be obtained when the particle is not oriented parallel to the X-axis, which is the direction of the scan. For example, a single-line scan at $\theta = 0^{\circ}$ would provide less height data when compared to a singleline scan performed at $\theta = 135^{\circ}$ (see Fig. 10a). This is unfavorable as the accuracy of characterizing such particles is inherently tied to their width L_2 . As a suggestion, when implementing this methodology in the experimental setup, one could circumvent this by programming the XY-stage to perform a single-line scan along the longest length (i.e., L_1) of the particle. This will increase the amount of height data collected by the CCS and thereby increase the accuracy of the estimated thickness.

Based on the analysis presented in this section on the *single-line scan*, we can safely make two statements. First, the *single-line scan* presents a faster approach (10–20 times when compared to *full scan*) to characterize the size and shape of thousands cuboidal particles. Second, and most importantly, despite the inability to fully reconstruct the particles in 3D, the *single-line scan* offers qualitatively similar measurement accuracy when compared to the *full scan*. Note that irrespective of the mode of operation of our proposed technique, the accuracy along the length and width dimensions will be unaffected as they are characterized by the camera, instead of the CCS.

6. Concluding remarks

6.1. Key outcomes

In this work, we have conceptualized, designed, built, and experimentally validated a fast and accurate offline approach to characterize the size and shape of cuboidal particles. Commercial techniques that have the potential to tackle such a characterization often suffer from slow data acquisition and optical issues. Except for dual-projection imaging setups, like the DISCO [76], most imaging devices developed in academia measure at most two characteristic lengths. They additionally suffer from issues arising from poor image quality, overlapping particles in dense suspensions, and particle orientation with respect to the imaging plane. We have tried to address most, if not all, of the aforementioned problems. To conclude, the key outcomes from this work can be summarized as follows:

- three characteristic lengths (length, width, and thickness) of ensembles of cuboidal particles can be accurately obtained by employing a combination of imaging and chromatic confocal microscopy
- characterization of the size and shape of cuboidal particles can be achieved in a practical amount of time and in theory faster than existing commercial techniques
- issues associated with particle orientation and high suspension densities – that often plague online imaging tools – can be eliminated by using an offline characterization tool coupled with a robust dry powder disperser

6.2. Key limitations

We acknowledge that despite the accurate characterization of the size and shape, as evidenced by the analysis presented in this work, the following limitations with our proposed technique must be kept in mind:

- Both the single-line scan and full scan can lead to incorrect height measurements due to hardware limitations when facets of crystalline particles exhibit steep angles with the substrate (in excess of 20°)
- Our technique cannot be used to obtain high time-resolution data in real-time, in contrast to techniques like the DISCO [76].
 This can potentially have implications in its eventual application in reliably extracting multidimensional kinetic parameters for crystallization phenomena
- The CCS technique depends on the strength of the light reflected from the surface. This will lead to noise in the signal arising from the irregular surface of crystals, which can potentially affect the 3D reconstruction and the estimation of particle thickness

Despite the aforementioned limitations, it should be evident that the proposed technique is a powerful addition in the toolbox for anyone who works on particulate matter. The technique can aid in troubleshooting processes that suffer from poor particle sizes and shapes, by providing a fast and accurate characterization of the PSSD.

CRediT authorship contribution statement

Petros Neoptolemou: Conceptualization, Methodology, Software, Validation, Formal analysis, Investigation, Visualization, Writing – original draft. Thomas Vetter: Conceptualization, Methodology, Writing – review & editing, Supervision, Funding acquisition. Aurora J. Cruz-Cabeza: Methodology, Writing – review & editing, Supervision. Ashwin Kumar Rajagopalan: Conceptualization, Methodology, Formal analysis, Investigation, Visualization, Writing – original draft, Supervision.

Declaration of competing interest

We do not have any financial interests or personal relationships with EPSRC, Wellcome Trust, AstraZeneca and MSD. These bodies funded the PhD/equipment. If any, I would only have AstraZeneca and MSD in the list as the other two are funding agencies.

Data availability

Data will be made available on request.

Acknowledgments

This work was financially supported by the Engineering and Physical Sciences Research Council (Voucher number: 17100002), MSD, Switzerland, and AstraZeneca. We are thankful to Weronika Kras (University of Manchester) for performing the SEM measurements, the staff in the EM Core Facility in the Faculty of Biology, Medicine, and Health for their assistance and the Wellcome Trust for equipment grant support to the EM Core Facility. We would also like to thank Dr. Giulio Perini (formerly University of Manchester) for his guidance on the design and purchase of the presented technique; Dr. Lorenzo Codan (MSD), David Milne (AstraZeneca), and Dr. David Wilson (AstraZeneca) for the fruitful discussions.

Appendix A. Supplementary data

Additional information on the experimental setup; evaluation of 3D reconstruction of steel feeler gauges; definition of shape descriptors of binary projections; definition of particle size and shape distribution; and properties of 1D thickness and 3D particle size and shape distributions.

Supplementary material related to this article can be found online at https://doi.org/10.1016/j.powtec.2023.119032.

References

- [1] P. Neoptolemou, T. Vetter, A. Cruz-Cabeza, A.K. Rajagopalan, Combined imaging and chromatic confocal microscopy technique to characterize size and shape of ensembles of cuboidal particles, in: ChemRxiv, 2023, http://dx.doi.org/10. 26434/chemrxiv-2023-nw1hs. (Accessed 19 July 2023).
- [2] S.J. Blott, K. Pye, Particle size distribution analysis of sand-sized particles by laser diffraction: An experimental investigation of instrument sensitivity and the effects of particle shape, Sedimentology 53 (2006) 671–685.
- [3] C. Servais, R. Jones, I. Roberts, The influence of particle size distribution on the processing of food, J. Food Eng. 51 (2002) 201–208.
- [4] J.H. Dane, C.G. Topp, Methods of Soil Analysis, Part 4: Physical Methods, Vol. 20, John Wiley & Sons, 2020.
- [5] K. Carpenter, W. Wood, Industrial crystallization for fine chemicals, Adv. Powder Technol. 15 (2004) 657–672.
- [6] R.A. Pearson, A.F. Yee, Influence of particle size and particle size distribution on toughening mechanisms in rubber-modified epoxies, J. Mater. Sci. 26 (1991) 3828–3844.
- [7] R. Chantrell, J. Popplewell, S. Charles, Measurements of particle size distribution parameters in ferrofluids, IEEE Trans. Magn. 14 (1978) 975–977.
- [8] H.Y. Sohn, C. Moreland, The effect of particle size distribution on packing density, Can. J. Chem. Eng. 46 (1968) 162–167.
- [9] J. Gan, Z. Zhou, A. Yu, Effect of particle shape and size on effective thermal conductivity of packed beds, Powder Technol. 311 (2017) 157–166.
- [10] G. Perini, F. Salvatori, D.R. Ochsenbein, M. Mazzotti, T. Vetter, Filterability prediction of needle-like crystals based on particle size and shape distribution data, Sep. Purif. Technol. 211 (2019) 768–781.
- [11] G. Perini, C. Avendaño, W. Hicks, A.R. Parsons, T. Vetter, Predicting filtration of needle-like crystals: A Monte Carlo simulation study of polydisperse packings of spherocylinders, Chem. Eng. Sci. (2021).
- [12] W.-L. Wu, C. Chappelow, N. Hanspal, P. Larsen, J. Patton, A. Shinkle, Z.K. Nagy, Implementation and application of image analysis-based turbidity direct nucleation control for rapid agrochemical crystallization process design and scale-up, Ind. Eng. Chem. Res. 61 (39) (2022) 14561–14572.
- [13] N. Sandler, D. Wilson, Prediction of granule packing and flow behavior based on particle size and shape analysis, J. Pharm. Sci. 99 (2009).
- [14] N. Pudasaini, P.P. Upadhyay, C.R. Parker, S.U. Hagen, A.D. Bond, J. Rantanen, Downstream processability of crystal habit-modified active pharmaceutical ingredient, Org. Process Res. Dev. 21 (2017) 571–577.
- [15] S. Tan, J. Newton, Powder flowability as an indication of capsule filling performance, Int. J. Pharm. 61 (1990) 145–155.
- [16] J.G. Osorio, F.J. Muzzio, Effects of powder flow properties on capsule filling weight uniformity, Drug Dev. Ind. 39 (2013) 1464–1475.
- [17] N. Rasenack, B.W. Müller, Crystal habit and tableting behavior, Int. J. Pharm. 244 (2002) 45–57.
- [18] R. Hintz, K. Johnson, The effect of particle size distribution on dissolution rate and oral absorption, Int. J. Pharm. 51 (1989) 9-17.
- [19] M. Guo, Q. Fu, C. Wu, Z. Guo, M. Li, J. Sun, Z. He, L. Yang, Rod shaped nanocrystals exhibit superior in vitro dissolution and in vivo bioavailability over spherical like nanocrystals: A case study of lovastatin, Colloids Surf. B. 128 (2015) 410–418.
- [20] P. Li, G. He, D. Lu, X. Xu, S. Chen, X. Jiang, Crystal size distribution and aspect ratio control for rodlike urea crystal via two-dimensional growth evaluation, Ind. Eng. Chem. Res. 56 (2017) 2573–2581.
- [21] A.K. Rajagopalan, S. Bötschi, M. Morari, M. Mazzotti, Feedback control for the size and shape evolution of needle-like crystals in suspension. II. Cooling crystallization experiments, Cryst. Growth Des. 18 (2018) 6185–6196.
- [22] J.Y. Heng, F. Thielmann, D.R. Williams, The effects of milling on the surface properties of form I paracetamol crystals, Pharm. Res. 23 (2006) 1918–1927.
- [23] F. Salvatori, M. Mazzotti, Experimental characterization and mathematical modeling of breakage of needle-like crystals in a continuous rotor-stator wet mill, Cryst. Growth Des. 18 (2018) 5957–5972.
- [24] W. Meng, E. Sirota, H. Feng, J.P. McMullen, L. Codan, A.S. Cote, Effective control of crystal size via an integrated crystallization, wet milling, and annealing recirculation system, Org. Process Res. Dev. 24 (2020) 2639–2650.
- [25] R.C. Snyder, S. Veesler, M.F. Doherty, The evolution of crystal shape during dissolution: Predictions and experiments, Cryst. Growth Des. 8 (2008) 1100–1101.
- [26] M.A. Lovette, M. Muratore, M.F. Doherty, Crystal shape modification through cycles of dissolution and growth: Attainable regions and experimental validation, AIChE J. 58 (5) (2012) 1465–1474.
- [27] D. Wilson, M. Bunker, D. Milne, A. Jawor-Baczynska, A. Powell, J. Blyth, D. Streather, Particle engineering of needle shaped crystals by wet milling and temperature cycling: Optimisation for roller compaction, Powder Technol. 339 (2018) 641–650.
- [28] A. Eren, B. Szilagyi, J.L. Quon, C.D. Papageorgiou, Z.K. Nagy, Experimental investigation of an integrated crystallization and wet-milling system with temperature cycling to control the size and aspect ratio of needle-shaped pharmaceutical crystals, Cryst. Growth Des. 21 (2021) 3981–3993.

- [29] J. Garside, M.B. Shah, Crystallization kinetics from MSMPR crystallizers, Ind. Eng. Chem. Process Des. Dev. 19 (4) (1980) 509–514.
- [30] N. Kubota, Effect of impurities on the growth kinetics of crystals, Cryst. Res. Technol. 36 (2001) 749–769.
- [31] T. Vetter, M. Mazzotti, J. Brozio, Slowing the growth rate of ibuprofen crystals using the polymeric additive pluronic F127, Cryst. Growth Des. 11 (9) (2011) 3813–3821.
- [32] E. Simone, A.R. Klapwijk, C.C. Wilson, Z.K. Nagy, Investigation of the evolution of crystal size and shape during temperature cycling and in the presence of a polymeric additive using combined process analytical technologies, Cryst. Growth Des. (2017).
- [33] C.A. Offiler, C.P. Fonte, W. Kras, P. Neoptolemou, R.J. Davey, T. Vetter, A.J. Cruz-Cabeza, Complex growth of benzamide form I: Effect of additives, solution flow, and surface rugosity, Cryst. Growth Des. 22 (10) (2022) 6248–6261.
- [34] A.F. Silva, A. Burggraeve, Q. Denon, P.V.D. Meeren, N. Sandler, T.V.D. Kerkhof, M. Hellings, C. Vervaet, J.P. Remon, J.A. Lopes, T.D. Beer, Particle sizing measurements in pharmaceutical applications: Comparison of in-process methods versus off-line methods, Eur. J. Pharm. Biopharm. 85 (2013) 1006–1018.
- [35] A. Ruf, J. Worlitschek, M. Mazzotti, Modeling and experimental analysis of PSD measurements through FBRM, Part. Part. Syst. Charact. 17 (4) (2000) 167–179.
- [36] E. Hishamuddin, A.G. Stapley, Z.K. Nagy, Application of laser backscattering for monitoring of palm oil crystallisation from melt, J. Cryst. Growth 335 (1) (2011) 172–180.
- [37] E. Simone, W. Zhang, Z.K. Nagy, Application of process analytical technology-based feedback control strategies to improve purity and size distribution in biopharmaceutical crystallization, Cryst. Growth Des. 15 (6) (2015) 2908–2919.
- [38] R. Irizarry, A. Chen, R. Crawford, L. Codan, J. Schoell, Data-driven model and model paradigm to predict 1D and 2D particle size distribution from measured chord-length distribution, Chem. Eng. Sci. 164 (2017) 202–218.
- [39] O.S. Agimelen, A.J. Mulholland, J. Sefcik, Modelling of artefacts in estimations of particle size of needle-like particles from laser diffraction measurements, Chem. Eng. Sci. 158 (2017) 445–452.
- [40] M. Li, D. Wilkinson, Determination of non-spherical particle size distribution from chord length measurements. Part 1: Theoretical analysis, Chem. Eng. Sci. 60 (12) (2005) 3251–3265.
- [41] M. Li, D. Wilkinson, K. Patchigolla, Determination of non-spherical particle size distribution from chord length measurements. Part 2: Experimental validation, Chem. Eng. Sci. 60 (18) (2005) 4992–5003.
- [42] D. Petrak, S. Dietrich, G. Eckardt, M. Köhler, Two-dimensional particle shape analysis from chord measurements to increase accuracy of particle shape determination, Powder Technol. 284 (2015) 25–31.
- [43] D.A. Ramirez-Quintero, W.A. Bizzo, Experimental characterization of the size, shape and ash composition of solid particles from different biomasses and separated by elutriation, Biomass Bioenergy 172 (2023) 106767.
- [44] I. de Albuquerque, M. Mazzotti, D.R. Ochsenbein, M. Morari, Effect of needlelike crystal shape on measured particle size distributions, AIChE J. 62 (2016) 2974–2985
- [45] S.J. Blott, K. Pye, Particle shape: A review and new methods of characterization and classification, Sedimentology 55 (1) (2008) 31–63.
- [46] T.E. Arnaout, L. Kurki, T. Vaarala, K. Ojala, P. Cullen, C. Sullivan, Crystallization monitoring using simultaneous bright field and PlasDIC imaging, J. Chem. Eng. 300 (2016) 64–74.
- [47] P. Neoptolemou, N. Goyal, A.J. Cruz-Cabeza, A.A. Kiss, D.J. Milne, T. Vetter, A novel image analysis technique for 2D characterization of overlapping needle-like crystals, Powder Technol. 399 (2022) 116827.
- [48] M. Kempkes, T. Vetter, M. Mazzotti, Measurement of 3D particle size distributions by stereoscopic imaging, Chem. Eng. Sci. 65 (2010) 1362–1373.
- [49] P.A. Larsen, J.B. Rawlings, N.J. Ferrier, Model-based object recognition to measure crystal size and shape distributions from in situ video images, Chem. Eng. Sci. 62 (2007) 1430–1441.
- [50] S. Schorsch, T. Vetter, M. Mazzotti, Measuring multidimensional particle size distributions during crystallization, Chem. Eng. Sci. 77 (2012) 130–142.
- [51] A.K. Rajagopalan, J. Schneeberger, F. Salvatori, S. Bötschi, D.R. Ochsenbein, M.R. Oswald, M. Pollefeys, M. Mazzotti, A comprehensive shape analysis pipeline for stereoscopic measurements of particulate populations in suspension, Powder Technol. 321 (2017) 479–493.
- [52] A. Borsos, A. Majumder, Z.K. Nagy, Multi-impurity adsorption model for modeling crystal purity and shape evolution during crystallization processes in impure media, Cryst. Growth Des. 16 (2016) 555–568.
- [53] D.R. Ochsenbein, S. Schorsch, T. Vetter, M. Mazzotti, M. Morari, Growth rate estimation of β l-glutamic acid from online measurements of multidimensional particle size distributions and concentration, Ind. Eng. Chem. Res. 53 (2014) 9136–9148.
- [54] F. Salvatori, P. Binel, M. Mazzotti, Efficient assessment of combined crystallization, milling, and dissolution cycles for crystal size and shape manipulation, Chem. Eng. Sci.: X 1 (2019) 100004.
- [55] S. Bötschi, A.K. Rajagopalan, M. Morari, M. Mazzotti, An alternative approach to estimate solute concentration: Exploiting the information embedded in the solid phase, J. Phys. Chem. Lett. 9 (2018) 4210–4214.

- [56] S. Bötschi, A.K. Rajagopalan, M. Morari, M. Mazzotti, Feedback control for the size and shape evolution of needle-like crystals in suspension. IV. Modeling and control of dissolution, Cryst. Growth Des. 19 (2019) 4029–4043.
- [57] A.K. Rajagopalan, S. Bötschi, M. Morari, M. Mazzotti, Feedback control for the size and shape evolution of needle-like crystals in suspension. III. Wet milling, Cryst. Growth Des. 19 (2019) 2845–2861.
- [58] B. Szilágyi, A. Eren, J.L. Quon, C.D. Papageorgiou, Z.K. Nagy, Monitoring and digital design of the cooling crystallization of a high-aspect ratio anticancer drug using a two-dimensional population balance model, Chem. Eng. Sci. 257 (2022) 117700.
- [59] S. Bötschi, A.K. Rajagopalan, I. Rombaut, M. Morari, M. Mazzotti, From needlelike toward equant particles: A controlled crystal shape engineering pathway, Comput. Chem. Eng. 131 (2019).
- [60] D.M. Scott, Recent advances in in-process characterization of suspensions and slurries, Powder Technol. 399 (2022) 117159.
- [61] J. Liu, W. Kuang, J. Liu, Z. Gao, S. Rohani, J. Gong, In-situ multi-phase flow imaging for particle dynamic tracking and characterization: Advances and applications, J. Chem. Eng. 438 (2022) 135554.
- [62] U. Ulusoy, A review of particle shape effects on material properties for various engineering applications: From macro to nanoscale, Minerals 13 (1) (2023).
- [63] H. Singh, A.M. Gokhale, Visualization of three-dimensional microstructures, Mater. Charact. 54 (2005) 21–29.
- [64] H. Abdullahi, P. Neoptolemou, C.L. Burcham, T. Vetter, Single droplets to particles - size, shape, shell thickness and porosity analyses using X-ray computed tomography, Chem. Eng. Sci. 245 (2021).
- [65] S.A. Schiele, F. Antoni, R. Meinhardt, H. Briesen, Analysis of nonideal shape evolution during potash alum crystallization using microcomputed tomography and three-dimensional image analysis, Cryst. Growth Des. 21 (2021) 1751–1761.
- [66] S.A. Schiele, F. Antoni, R. Meinhardt, H. Briesen, Analysis of nonideal shape evolution during potash alum crystallization using microcomputed tomography and three-dimensional image analysis, Cryst. Growth Des. 21 (2021) 1751–1761.
- [67] B. Zhou, J. Wang, H. Wang, Three-dimensional sphericity, roundness and fractal dimension of sand particles, Géotechnique 68 (1) (2018) 18–30.
- [68] J.W. Bullard, E.J. Garboczi, Defining shape measures for 3D star-shaped particles: Sphericity, roundness, and dimensions, Powder Technol. 249 (2013) 241–252.
- [69] B. Bujak, M. Bottlinger, Three-dimensional measurement of particle shape, Part. Part. Syst. Charact. 25 (2008) 293–297.
- [70] G. Bagheri, C. Bonadonna, I. Manzella, P. Vonlanthen, On the characterization of size and shape of irregular particles, Powder Technol. 270 (2015) 141–153.

- [71] O. Kemppinen, Y. Heinson, M. Berg, Quasi-three-dimensional particle imaging with digital holography, Appl. Opt. 56 (2017) F53–F60.
- [72] M.R. Singh, J. Chakraborty, N. Nere, H.-H. Tung, S. Bordawekar, D. Ramkrishna, Image-analysis-based method for 3D crystal morphology measurement and polymorph identification using confocal microscopy, Cryst. Growth Des. 12 (2012) 3735–3748.
- [73] V. Bullman, Automated three-dimensional analysis of particle measurements using an optical profilometer and image analysis software, J. Microsc. 211 (2003) 95–100.
- [74] A.D. Elliott, Confocal microscopy: Principles and modern practices, Curr. Protoc. Cytom. 92 (2020).
- [75] A. Jaeggi, A.K. Rajagopalan, M. Morari, M. Mazzotti, Characterizing ensembles of platelike particles via machine learning, Ind. Eng. Chem. Res. 60 (2021) 473–483.
- [76] P. Binel, A. Jain, A. Jaeggi, D. Biri, A.K. Rajagopalan, A.J. deMello, M. Mazzotti, Online 3D characterization of micrometer-sized cuboidal particles in suspension, Small Methods 2201018.
- [77] M.A. Browne, O. Akinyemi, A. Boyde, Confocal surface profiling utilizing chromatic aberration, Scanning 14 (1992) 145–153.
- [78] F. Blateyron, Chromatic confocal microscopy, in: R. Leach (Ed.), Optical Measurement of Surface Topography, Springer Berlin Heidelberg, Berlin, Heidelberg, 2011, pp. 71–106.
- [79] H.J. Tiziani, H.-M. Uhde, Three-dimensional image sensing by chromatic confocal microscopy, Appl. Opt. 33 (1994) 1838–1843.
- [80] MATLAB 9.10 and Image Processing Toolbox 11.3, The MathWorks, Natick, MA, USA, 2021.
- [81] N. Otsu, A threshold selection method from gray-level histograms, IEEE Trans. Syst. Man Cybern. Syst. 9 (1979) 62–66.
- [82] MATLAB 9.10 and Computer Vision Toolbox 10.0, The MathWorks, Natick, MA, USA, 2021.
- [83] P. Sacchi, S.M. Reutzel-Edens, A.J. Cruz-Cabeza, The unexpected discovery of the ninth polymorph of tolfenamic acid, CrystEngComm 23 (2021) 3636–3647.
- [84] L.M. Jawerth, S. Münster, D.A. Vader, B. Fabry, D.A. Weitz, A blind spot in confocal reflection microscopy: The dependence of fiber brightness on fiber orientation in imaging biopolymer networks, Biophys. J. 98 (3) (2010) L1–L3.
- [85] R. Gunawan, D.L. Ma, M. Fujiwara, R.D. Braatz, Identification of kinetic parameters in multidimensional crystallization processes, Internat. J. Modern Phys. B 16 (01n02) (2002) 367–374.
- [86] S. Bötschi, A.K. Rajagopalan, M. Morari, M. Mazzotti, Feedback control for the size and shape evolution of needle-like crystals in suspension. IV. Modeling and control of dissolution, Cryst. Growth Des. 19 (2019) 4029–4043.